

Cortical actin contributes to spatial organization of ER–PM junctions

Ting-Sung Hsieh, Yu-Ju Chen, Chi-Lun Chang, Wan-Ru Lee, and Jen Liou*

Department of Physiology, University of Texas Southwestern Medical Center, Dallas, TX 75390

ABSTRACT Endoplasmic reticulum–plasma membrane (ER–PM) junctions mediate crucial activities ranging from Ca^{2+} signaling to lipid metabolism. Spatial organization of ER–PM junctions may modulate the extent and location of these cellular activities. However, the morphology and distribution of ER–PM junctions are not well characterized. Using photoactivated localization microscopy, we reveal that the contact area of single ER–PM junctions is mainly oblong with the dimensions of $\sim 120 \text{ nm} \times \sim 80 \text{ nm}$ in HeLa cells. Using total internal reflection fluorescence microscopy and structure illumination microscopy, we show that cortical actin contributes to spatial distribution and stability of ER–PM junctions. Further functional assays suggest that intact F-actin architecture is required for phosphatidylinositol 4,5-bisphosphate homeostasis mediated by Nir2 at ER–PM junctions. Together, our study provides quantitative information on spatial organization of ER–PM junctions that is in part regulated by F-actin. We envision that functions of ER–PM junctions can be differentially regulated through dynamic actin remodeling during cellular processes.

Monitoring Editor

Jennifer Lippincott-Schwartz
Howard Hughes Medical
Institute

Received: Jun 14, 2017

Revised: Sep 18, 2017

Accepted: Sep 20, 2017

INTRODUCTION

Endoplasmic reticulum–plasma membrane (ER–PM) junctions exist in most, if not all, eukaryotic cells. In mammalian cells, ER–PM junctions serve as platforms for both STIM1/Orai1-mediated store-operated Ca^{2+} entry (SOCE) and nonvesicular lipid transfer (Okeke *et al.*, 2016; Chang *et al.*, 2017; Saheki and De Camilli, 2017). Given structure–function coupling in biological systems, regulation of the spatial organization of ER–PM junctions will likely have direct consequences for these cellular functions. Such

regulation may be introduced by ER shaping proteins (Jozsef *et al.*, 2014), junctional tethers (Chang *et al.*, 2013; Giordano *et al.*, 2013), and cortical cytoskeleton (Dingsdale *et al.*, 2013; Wang *et al.*, 2014; Zhang *et al.*, 2016; van Vliet *et al.*, 2017). Particularly, actin forms cortical meshwork (Morone *et al.*, 2006) that may potentially determine the extent and location of ER–PM junctions. Nevertheless, the morphology and distribution of ER–PM junctions, as well as the machinery regulating these properties, remain underexplored.

The main obstacle to studying junctional morphology is that it is difficult to visualize these miniature structures without electron microscopy (EM). Traditional transmission EM (TEM) analysis can obtain only a one-dimensional (1D) estimation for 2D morphological features of the contact area between the ER and the PM. Though such features can be retrieved by 3D EM techniques (West *et al.*, 2011; Fernandez-Busnadiego *et al.*, 2015; Wu *et al.*, 2017), the attainable sample size is often limited. As for investigating junctional distribution, the major difficulty lies in identification of a fluorescent marker that can selectively reveal ER–PM junctions without perturbing their native architecture.

To overcome these limitations, we developed a genetically encoded marker called “MAPPER” that allows visualization of ER–PM junctions using various imaging techniques (Chang *et al.*, 2013). Here we applied MAPPER to study the morphology and subcellular distribution of single ER–PM junctions using super-/high-resolution imaging together with quantitative analysis.

This article was published online ahead of print in MBoC in Press (<http://www.molbiolcell.org/cgi/doi/10.1091/mbc.E17-06-0377>) on September 27, 2017.

Author contributions: T.S.H., C.L.C., and J.L. conceived and designed the study. C.L.C. contributed new reagents. T.S.H., Y.J.C., and W.R.L. performed experiments and image and data analysis. T.S.H. and J.L. wrote the manuscript.

*Address correspondence to: Jen Liou (jen.liou@utsouthwestern.edu).

Abbreviations used: DBSCAN, density-based spatial clustering of applications with noise; EM, electron microscopy; ER, endoplasmic reticulum; His, histamine; IQR, interquartile range; LatB, latrunculin B; MSD, mean square displacement; NN, nearest-neighbor; PALM, photoactivated localization microscopy; PI(4,5)P₂, phosphatidylinositol 4,5-bisphosphate; PM, plasma membrane; SIM, structure illumination microscopy; SOCE, store-operated Ca^{2+} entry; TEM, transmission EM; Tg, thapsigargin; TIRFM, total internal reflection fluorescence microscopy.

© 2017 Hsieh *et al.* This article is distributed by The American Society for Cell Biology under license from the author(s). Two months after publication it is available to the public under an Attribution–Noncommercial–Share Alike 3.0 Unported Creative Commons License (<http://creativecommons.org/licenses/by-nc-sa/3.0>).

“ASCB®,” “The American Society for Cell Biology®,” and “Molecular Biology of the Cell®” are registered trademarks of The American Society for Cell Biology.

RESULTS AND DISCUSSION

PALM resolves morphology of the contact area of individual ER-PM junctions

Previous and our TEM analyses suggest that the size of native ER-PM junctions in nonexcitable mammalian cells is below the diffraction barrier of conventional light microscopy (Wu *et al.*, 2006; Orci *et al.*, 2009; Supplemental Figure S1, A and B). We thus used the super-resolution imaging technique photoactivated localization microscopy (PALM) and the junctional marker tdEos4-MAPPER for resolving fine structures of the contact area of ER-PM junctions. tdEos4-MAPPER provides high labeling density for ER-PM junctions even when moderately expressed, thus minimizing potential overexpression artifacts. Compared with total internal reflection fluorescence microscopy (TIRFM), PALM better resolved single ER-PM junctions labeled by tdEos4-MAPPER (Figure 1A and Supplemental Figure S1C). Adjacent junctions were separated (Figure 1A, boxed region 1), and morphological heterogeneity of individual junctions became clearly visible (Figure 1A, boxed region 2) in PALM images.

To quantitatively characterize morphology of the contact area of ER-PM junctions, we used an integrated software platform developed by Levet *et al.* (2015). This platform implements spatial point analysis methods directly using molecule localizations of PALM data, avoiding often hard-to-reproduce intensity-based analysis using PALM images reconstructed by Gaussian rendering. We first performed Ripley's *K* analysis to estimate the size of ER-PM junctions. Theoretical evaluation has shown that the radius of maximal aggregation H_{\max} derived from Ripley's *K* analysis falls between the radius and the diameter of well-separated, disk-shaped clusters (Kiskowski *et al.*, 2009). We determined H_{\max} to be 123.5 ± 13.5 nm from PALM data of 30 cells (median \pm semi-interquartile range [IQR]; Figure 1B), in the same order of magnitude as the measurement obtained from TEM analysis. Because H_{\max} only provided a 1D, overall estimate of the junctional size, we thus sought for single junction quantification using the same data set. Recently, a Voronoi-tessellation-based framework called "SR-Tesseler" has been demonstrated to be robust in segmenting/quantifying PALM data (Levet *et al.*, 2015). We

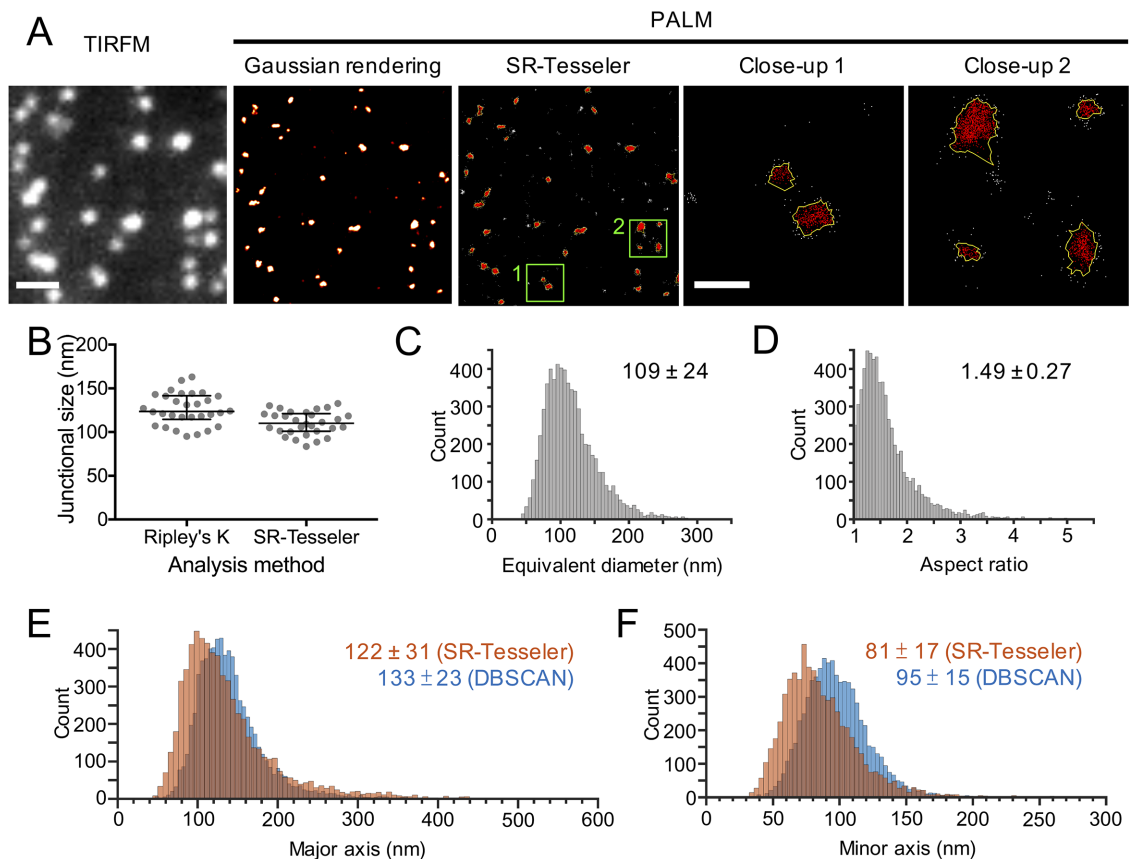


FIGURE 1: PALM resolves morphology of the contact area of individual ER-PM junctions. (A) Adherent surface of a HeLa cell transiently expressing tdEos4-MAPPER was imaged by TIRFM and PALM. PALM images reconstructed by Gaussian rendering and segmented by SR-Tesseler are shown. Molecule localizations within segmented ER-PM junctions are in red and segmentation outlined in yellow, whereas noises or incompletely labeled junctions are in white. Bars: 1 and 0.2 (close-ups) μm . (B) Ripley's *K* analysis and SR-Tesseler make comparable estimation about the size of ER-PM junctions. Radius of maximal aggregation evaluated by Ripley's *K* analysis and median equivalent diameter derived from SR-Tesseler were used in the comparison. Each point in the beeswarm plot represents a measurement derived from 1 cell, and bars represent median with IQR ($n = 30$). (C-F) The contact area of ER-PM junctions is mainly oblong with the dimensions of ~ 120 nm \times ~ 80 nm. Morphological properties of single junctions segmented by SR-Tesseler or DBSCAN are summarized as histograms (SR-Tesseler: C-F; DBSCAN: E and F). Insets: median \pm semi-IQR ($n = 6437$ [SR-Tesseler], 7232 [DBSCAN] junctions from 30 cells; the top and the bottom 0.1% of data values not included in the histograms for better visualization).

applied SR-Tesseler and found it well segmented ER–PM junctions (Figure 1A). Morphological analysis of single junctions showed that the equivalent diameter of junctions was 109 ± 24 nm (median \pm semi-IQR, $n = 6437$ junctions from 30 cells; Figure 1C), consistent with the result of TEM analysis. Moreover, the analysis revealed previously uncharacterized 2D morphological features of the junctions. Our analysis showed that ER–PM junctions were elongated in shape with a median aspect ratio of 1.49 ± 0.27 (Figure 1D). In detail, the median lengths of major and minor axes of ER–PM junctions were 122 ± 31 nm and 81 ± 17 nm, respectively (Figure 1, E and F). To further verify the above analysis results, we used the well-established clustering algorithm “density-based spatial clustering of applications with noise (DBSCAN)” (Ester *et al.*, 1996) to segment and quantify our PALM data. Though DBSCAN is prone to background noise present in PALM data (Nan *et al.*, 2013) and demands careful parameter optimization, a proper choice of parameters generated results comparable to SR-Tesseler (Figure 1, E and F).

In sum, PALM uncovers previously unappreciated morphological heterogeneity of ER–PM junctions masked by the diffraction of light. Moreover, single junction quantification shows that ER–PM junctions are mainly oblong with the dimensions of ~ 120 nm \times ~ 80 nm. Such junctional morphology and its heterogeneity may be due to types/abundance of ER shaping proteins or molecular tethers at individual junctions. The organization of cortical cytoskeleton may also confine the junctional size because it is energetically unfavorable for a junction to break through barriers set by cortical cytoskeleton.

TIRFM and TIRF-SIM reveal spatial coordination of ER–PM junctions and cortical actin

Next, we investigated the distribution of ER–PM junctions in the cell. Because F-actin plays a pivotal role in the organization of cell cortex, we examined whether there is spatial coordination of ER–PM junctions and cortical actin. Using TIRFM, we observed that ER–PM junctions were precluded from the regions with dense F-actin networks or thick stress fibers in cells expressing MAPPER and stained with Alexa Fluor 568-Phalloidin to reveal native F-actin architecture (Figure 2A). We also noticed that the junctions sometimes aligned along cortical actin (Figure 2A, white arrows). Further computational analysis showed that most of the junctions were not superimposed on, but in close proximity to, F-actin (Figure 2, B and C), supporting the idea that there is spatial coordination of ER–PM junctions and cortical actin. To better corroborate these observations, we then used the super-resolution imaging technique total internal reflection fluorescence structure illumination microscopy (TIRF-SIM) because the intricate architecture of cortical actin is usually within the diffraction limit (Morone *et al.*, 2006; Xu *et al.*, 2012; Eghiaian *et al.*, 2015; Kronlage *et al.*, 2015). Increased lateral resolution of TIRF-SIM images revealed fine structural details of cortical actin (Figure 2D). Apparently, fewer ER–PM junctions distributed in the region with dense actin meshwork (Figure 2D, yellow arrow) and the junctions mainly located in the mesh or open space between two nearby F-actin structures (Figure 2D, close-ups). Consistent with TIRFM data, most of the junctions were not superimposed on, but in close proximity to, F-actin (Figure 2, E and F). These results suggest that there is spatial coordination via direct or indirect interplay between ER–PM junctions and cortical actin, in support of previous studies (Dingsdale *et al.*, 2013; van Vliet *et al.*, 2017). It is of note that spatial coupling of ER–PM junctions and F-actin has also been shown in plant cells (Wang *et al.*, 2014), where the ER is associated with F-actin.

Cortical actin contributes to spatial organization of ER–PM junctions

To better understand the role of cortical actin in spatial organization of ER–PM junctions, we performed pharmacological perturbations using the actin polymerization inhibitor latrunculin B (LatB). We found that the lateral motility of junctions increased in LatB-treated cells (Figure 3A and Supplemental Movie S1). Trajectory analysis showed that, for ER–PM junctions that could be tracked for ≥ 5 min, LatB treatment increased the median of mean velocities of junctional trajectories from 0.18 to 0.35 $\mu\text{m}/\text{min}$ (Figure 3B). Moreover, mean square displacement (MSD) analysis showed that LatB treatment increased the diffusion coefficient of ER–PM junctions from 3.8×10^{-3} to 9.1×10^{-3} $\mu\text{m}^2/\text{min}$ (Figure 3C), implying the junctions become more diffusive after LatB treatment. We also found that ER–PM junctions became more morphologically heterogeneous and underwent apparent fusion/fission in some LatB-treated cells (Supplemental Movie S1C). This phenomenon might result from junctional clumping due to disruption of F-actin by LatB (Supplemental Movie S2). Together, these results suggest that cortical actin constrains motility of ER–PM junctions, either by preventing PM-associated ER strands moving laterally or by limiting relative motion of junctional tethers.

We noticed that some ER–PM junctions underwent dissolution during disruption of F-actin by LatB (Supplemental Movie S2). We thus investigated the role of cortical actin in stability of ER–PM junctions. Strikingly, LatB treatment caused a 35% reduction of junctional density (Figure 4A), suggesting that cortical actin supports junctional formation or enhance their stability. We also assessed the role of cortical actin in spatial distribution of ER–PM junctions using nearest-neighbor (NN) analysis. In NN analysis, the distance between one junction to its nearest neighbor is determined and defined as its NN distance. The overall profiles of NN distance allow one to quantitatively compare spatial distribution of the junctions between cell populations. As LatB treatment reduced the density of ER–PM junctions, NN distance of the junctions was correspondingly increased (Figure 4, B and C). Besides, LatB treatment increased the variability of NN distance of the junctions (Figure 4D), indicating that intracellular organization of ER–PM junctions was compromised by LatB treatment. We further used the Clark–Evans measure to test spatial randomness of the junctional distribution (Clark and Evans, 1954). The Clark–Evans measure is expected to be 1 for a spatially random distribution, with values significantly greater or smaller than 1 indicating dispersed or clustered distributions, respectively. We found that the Clark–Evans measures for most of the cells in both control and LatB groups were significantly greater than 1 (Figure 4E), indicating that cellular distribution of ER–PM junctions was generally more dispersed than random, even when F-actin was disrupted. Together, these results suggest that cortical actin contributes to spatial distribution of ER–PM junctions, but other factors likely also exist to keep the junctions dispersed.

Disruption of F-actin impacts PI(4,5)P₂ homeostasis but not SOCE mediated by ER–PM junctions

Given the disorganization of ER–PM junctions in LatB-treated cells, we tested whether cellular activities mediated by ER–PM junctions were affected in these cells. Phosphatidic acid/phosphatidylinositol countertransport activity of Nir2 at ER–PM junctions (Chang *et al.*, 2013; Chang and Liou, 2015; Kim *et al.*, 2015) has been shown to play a part in replenishing PM phosphatidylinositol 4,5-bisphosphate (PI(4,5)P₂) following receptor-induced hydrolysis. We thus first evaluated the competence of Nir2 in translocating to ER–PM junctions and promoting PM PI(4,5)P₂ replenishment after receptor

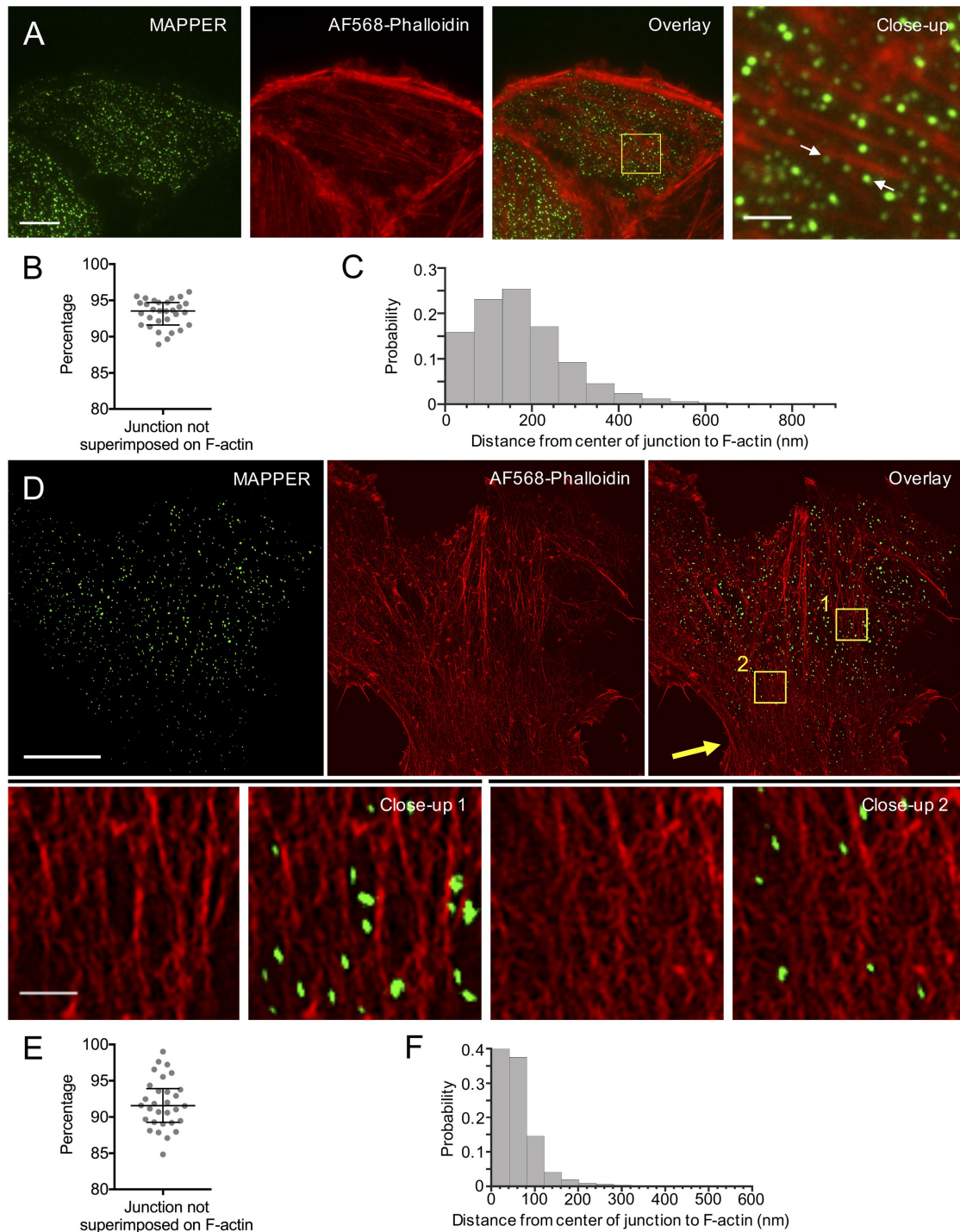


FIGURE 2: TIRFM and TIRF-SIM reveal spatial coordination of ER-PM junctions and cortical actin. (A) TIRFM images of a HeLa cell transiently expressing MAPPER and stained with the F-actin probe Alexa Fluor 568 (AF568)-phalloidin. An example of ER-PM junctions locally aligned along cortical actin is indicated by a pair of white arrows. Bars: 10 and 2 (close-up) μm . (B, C) Quantification of TIRFM images shows most of ER-PM junctions are not superimposed on, but in close proximity to, F-actin ($n = 36574$ junctions from 30 image crops). For B, each point in the beeswarm plot represents a measurement derived from 1 image crop, and bars represent median with IQR. For C, distances from center of junctions not colocalized with F-actin to the nearest F-actin structure are summarized as the histogram (the top and the bottom 0.1% of data values not included in the histogram for better visualization). (D) TIRF-SIM images of a HeLa cell stably expressing MAPPER and stained with AF568-phalloidin. The yellow arrow indicates a region with dense actin meshwork, where few ER-PM junctions distribute. In the close-ups of boxed regions, it is clear that ER-PM junctions mainly reside in the places devoid of cortical actin. Bars: 10 and 1 (close-ups) μm . (E, F) Quantification of TIRF-SIM images shows most of ER-PM junctions are not superimposed on, but in close proximity to, F-actin ($n = 19,386$ junctions from 30 image crops). Details of data visualization are the same as described in B and C.

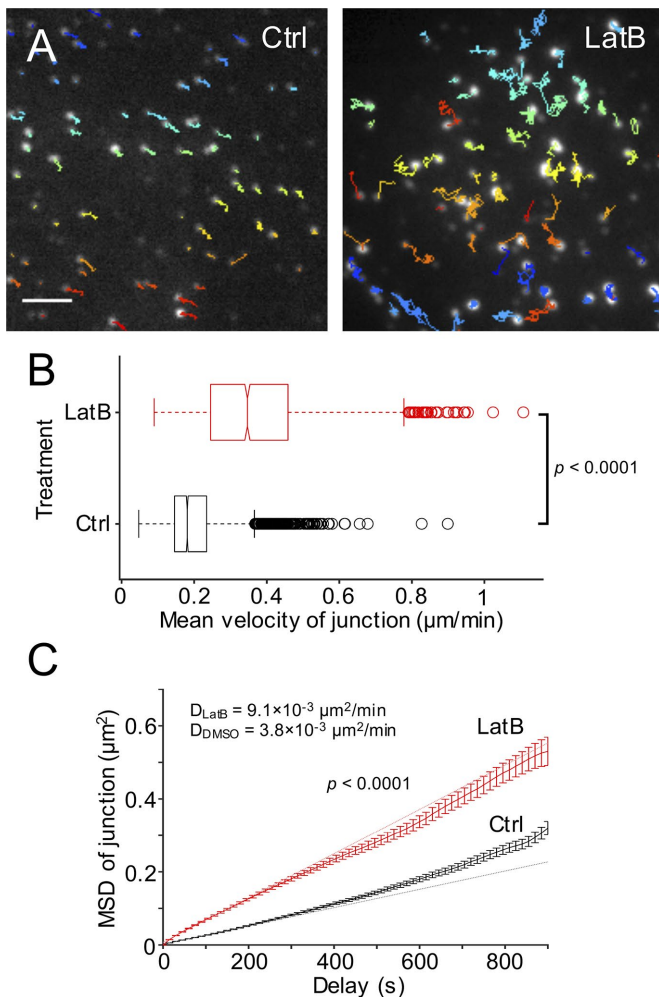


FIGURE 3: Disruption of F-actin by latrunculin B (LatB) enhances lateral motility of ER–PM junctions. HeLa cells stably expressing MAPPER were treated with vehicle control (Ctrl) or 5 μM LatB for 30 min before imaged with live-cell TIRFM. Lateral motion of individual junctions was tracked using Fiji/TrackMate ($n = 3426$, 2291 junctions being tracked for ≥ 5 min per condition from five independent experiments). (A) Representative images overlaid with junctional trajectories. Bar: 2 μm . (B) The box plot of mean velocities of junctional trajectories. Whiskers: Tukey style; notch: 95% CI for the median. p Value from unpaired two-tailed Welch’s t test was reported. (C) MSD curves of junctional motion. Solid lines: mean \pm SEM; dash lines: linear fit of initial 25% of mean MSD curves; inset: diffusion coefficients estimated by the abovementioned fit. p Value from unpaired two-tailed Student’s t test at each time delay except 0 was reported. See Supplemental Movie S1 for associated videos.

stimulation. In the majority of control cells, translocated Nir2 remained stable at the junctions after histamine stimulation (Figure 5, A and B, dynamics type N). In contrast, translocated Nir2 either failed to stay at ER–PM junctions (Figure 5, A and B, dynamics type A) or was spatially unstable (Figure 5, A and B, dynamics type B) in LatB-treated cells. We reasoned that stability and quantity of ER–PM junctions might affect the efficiency and capacity of Nir2-mediated lipid transport. Indeed, we observed that LatB treatment suppressed PM PI(4,5)P₂ replenishment following receptor stimulation (Figure 5C), likely caused by instability or density reduction of the junctions. Because ER–PM junctions are also crucial for SOCE mediated by STIM1/Orai1, we next evaluated the competence of STIM1

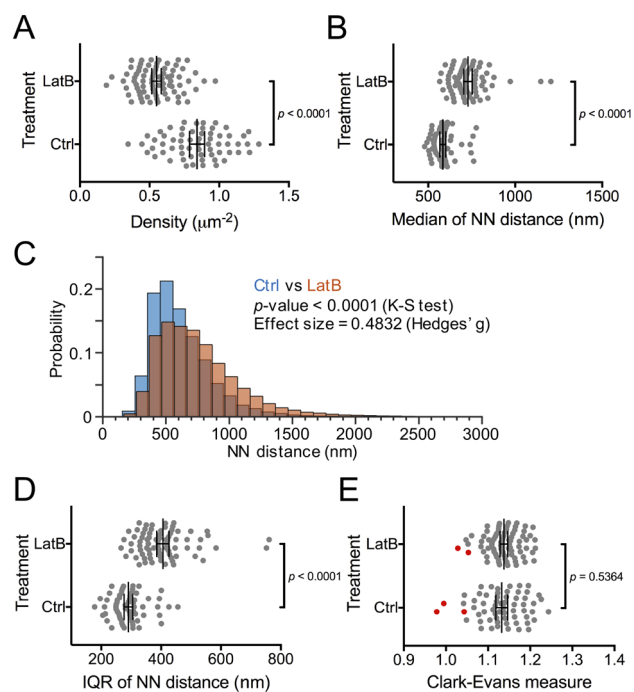


FIGURE 4: Disruption of F-actin by LatB alters the density and spatial distribution of ER–PM junctions. HeLa cells transiently expressing MAPPER and the PM marker mCherry-KRas-tail were treated with vehicle control or 5 μM LatB for 30 min before imaged with TIRFM. The junctional density in each cell and the nearest-neighbor (NN) distance of each junction were then quantified. For A, B, D, and E, each point in the beeswarm plots represents a measurement derived from 1 cell, and bars represent mean with 95% CI ($n = 62$, 77 cells per condition from three independent experiments). p Values from unpaired two-tailed Welch’s t test were reported. For C, NN distances of individual junctions are summarized as histograms (Ctrl, $n = 50,624$ junctions from 62 cells; LatB, $n = 42,621$ junctions from 77 cells; the top and the bottom 0.1% of data values not included in the histogram for better visualization). Hedges’ g was used to measure the effect size. Two-sample Kolmogorov–Smirnov (K-S) test was used to determine whether data distributions differ significantly. To account for hypersensitivity of K-S test with large sample sizes, 500 data points from each group were randomly subsampled for comparison in one iteration. The mean of p -values from 1000 iterations was reported. For E, the points with Clark–Evans measure not significantly deviated ($p > 0.05$, two-tailed Student’s t test) from 1 are in red.

in translocating to ER–PM junctions and mediating SOCE after depletion of ER Ca²⁺ store. Interestingly, the magnitude of STIM1 translocation after store depletion was not affected by LatB treatment (Figure 5, D and E), nor was SOCE (Figure 5F). Unlike Nir2, which is cytosolic and requires dual membrane targeting to be at the junctions, the SOCE mediators STIM1/Orai1 are transmembrane proteins and form oligomers during the interaction. Therefore, it could be that STIM1/Orai1 interaction is robust enough even when the junctions are destabilized. Together, our data demonstrate that intact F-actin architecture is required for PI(4,5)P₂ homeostasis mediated by Nir2 but not SOCE mediated by STIM1 at ER–PM junctions.

In conclusion, we provide systematic quantifications of spatial organization of ER–PM junctions using super- and high-resolution imaging in this work. We reveal that the contact area of single

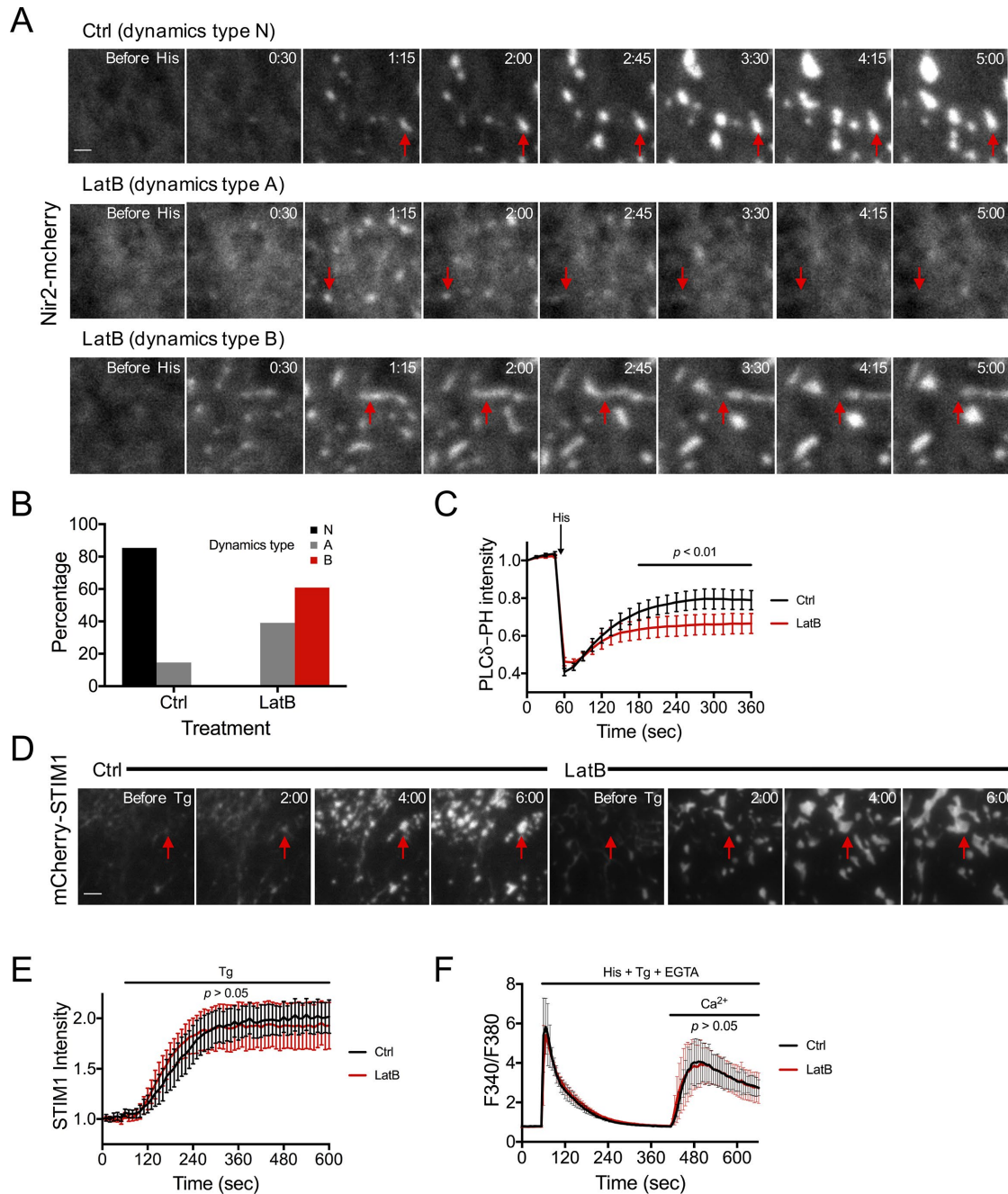


FIGURE 5: Intact F-actin architecture is required for PI(4,5)P₂ homeostasis mediated by Nir2 but not SOCE mediated by STIM1 at ER-PM junctions. (A, B) Disruption of F-actin by LatB decreases spatial stability of translocated Nir2 at ER-PM junctions. HeLa cells transiently expressing Nir2-mCherry and overexpressing H1R were treated with vehicle control or 5 μ M LatB for 15 min, and then Nir2 translocation to ER-PM junctions induced by 100 μ M histamine (His) was monitored with TIRFM. Red arrows mark the position of a Nir2 punctum appearing at 1:15 in each panel. Bar: 1 μ m. See Supplemental Movie S3 for associated videos. (B) The percentage of types N, A, B in Ctrl or LatB-treated cells ($n = 41, 46$ cells per condition). (C) Disruption of F-actin by LatB impedes PM PI(4,5)P₂ replenishment following receptor stimulation. HeLa cells transiently expressing GFP-PLC δ -PH and overexpressing H1R were treated with vehicle control or 5 μ M LatB and then change in PM GFP-PLC δ -PH intensity induced by 100 μ M His was monitored with TIRFM. Relative intensity changes are plotted. Curve and bars: mean with 95% CI ($n = 24, 17$ cells per condition, from three independent experiments). p Value from unpaired two-tailed Student's t test at each time point was reported. (D, E) Disruption of F-actin by LatB does not affect STIM1 translocation to ER-PM junctions following store depletion. HeLa cells transiently expressing mCherry-STIM1 and the PM marker YFP-KRas-tail were treated with vehicle control or 5 μ M LatB for 30 min, and then STIM1 translocation to ER-PM junctions induced by 1 μ M thapsigargin (Tg) was monitored with TIRFM. Red arrows mark the position of a STIM1 punctum appearing at 2:00 in each panel. Bar: 2 μ m. Relative changes in STIM1 intensity are plotted in E. Curve and bars: mean with 95% CI ($n = 15, 14$ cells per condition from two independent experiments). p Value from unpaired two-tailed Student's t test at each time point after Tg addition was reported. (F) Disruption of F-actin by LatB does not affect SOCE. HeLa cells were loaded with the Ca²⁺ indicator Fura-2, treated

junctions is generally oblong with the dimensions of ~120 nm × ~80 nm. We also reveal the dependence of junctional distribution on cortical actin architecture. Furthermore, we quantitatively show the importance of F-actin in spatial organization of ER–PM junctions and functional activities mediated by them. Our study deepens the understanding of how ER–PM junctions are spatially organized in the cell.

MATERIALS AND METHODS

Chemicals

Bovine serum albumin G418, histamine, latrunculin B, penicillin-streptomycin, dimethyl sulfoxide (DMSO), ethylene glycol-bis(2-aminoethylether)-*N,N,N',N'*-tetraacetic acid (EGTA), HCl, KOH and all chemicals for extracellular buffer (ECB: 125 mM NaCl, 5 mM KCl, 1.5 mM MgCl₂, 1.5 mM CaCl₂, 20 mM HEPES, 10 mM glucose, pH 7.4) were obtained from Sigma-Aldrich (St. Louis, MO). All chemicals for TEM experiments were obtained from Electron Microscopy Sciences (Hatfield, PA). Ethanol (200 proof) was obtained from Pharmco-Aaper (Brookfield, CT). Formaldehyde solution (16%), Fura2-AM, pluronic F-127, and thapsigargin were obtained from Thermo Fisher Scientific (Waltham, MA).

Cell culture

HeLa cells (American Type Culture Collection, Manassas, VA) were cultured in DMEM/high glucose with L-glutamine, sodium pyruvate (HyClone Laboratories, Logan, UT) supplemented with 10% fetal bovine serum (Sigma-Aldrich, St. Louis, MO), and 1% penicillin-streptomycin and incubated at 37°C with 5% CO₂. G418 (0.3 mg/ml) was supplemented to the culture medium for HeLa cells stably expressing MAPPER (1A5 clone).

DNA constructs

GFP-PLCδ-PH (Stauffer *et al.*, 1998), mCherry-STIM1 (Liou *et al.*, 2005), YFP-KRas-tail, mCherry-KRas-tail (Heo *et al.*, 2006), MAPPER, and Nir2-mCherry (Chang *et al.*, 2013) were previously described. tdEos4-MAPPER was generated by replacing GFP of MAPPER with tandem dimer of mEos4 variant mEos4-66 (Paez-Segala *et al.*, 2015) using the primers Agel-mEos4 F (5'-AT CGACCGGTC ATG GTG AGT GCG ATT AAG CC-3'), mEos4-Spel R (5'-A TCG ACTAGT TCG TCT GGC ATT GTC AGG-3'), and mEos4-3xSAGG-XmaI R (5'-ATC GCCCGGGGC ACC TCC GGC AGA GCC ACC TGC ACT GCC TCC AGC TGA TCG TCT GGC ATT GTC AGG-3'). All constructs were verified by sequencing.

TEM

HeLa cells and HeLa cells stably expressing MAPPER were seeded separately in 35-mm glass-bottom dishes (MatTek Corporation, Ashland, MA) at a density of 2×10^5 cells/dish ~16 h before fixation. Cells were fixed with 2.5% glutaraldehyde in buffer (0.1 M phosphate buffer with 0.2 M sucrose) for 10 min at room temperature (RT). Postfixation staining was performed with 1% osmium tetroxide/0.8% potassium ferricyanide in buffer for 1 h in the dark. After postfixation staining, cells were rinsed with buffer and water, stained en bloc with 2% uranyl acetate in water for 1 h, dehydrated through

graded series of ethanol, and then infiltrated and embedded with EMBED 812 resin. After embedding, coverslips were removed and blocks were trimmed. Ultrathin (60- to 70-nm) sections were cut using a microtome, mounted on formvar-coated grids, and imaged by a Tecnai G2 Spirit transmission electron microscope (FEI, Hillsboro, OR) equipped with a LaB₆ source operating at 120 keV.

PALM imaging

PALM imaging was performed with a DeltaVision OMX SR imaging system (GE Healthcare, Pittsburgh, PA) equipped with a PLAPON 60× oil objective (Olympus, Waltham, MA) and a pco.edge scientific complementary metal-oxide-semiconductor (sCMOS) camera (PCO-Tech, Romulus, MI).

For PALM imaging experiments, eight-well Nunc Lab-Tek II chambered coverglass (Thermo Fisher Scientific, Waltham, MA) was cleaned before seeding cells on it. Briefly, coverglass was sonicated in 1 M HCl for 30 min, rinsed with copious amounts of double-distilled water (ddH₂O), sonicated in ddH₂O for 5 min, sonicated in 1 M KOH for 30 min, rinsed with copious amounts of ddH₂O, sonicated in ddH₂O for 5 min, dipped in 70% ethanol, and then air-dried overnight in a clean and sterile environment. HeLa cells were seeded on cleaned coverglass at a density of 2×10^4 cells/well 1 d before transfection. tdEos4-MAPPER (50 ng/well) was transfected into cells with 0.1 μl/well of TransIT-X2 (Mirus Bio, Madison, WI) according to the manufacturer's instructions. Sixteen hours after transfection, cells were washed once with prewarmed phosphate-buffered saline (PBS) (HyClone Laboratories, Logan, UT) and then fixed with 4% formaldehyde in PBS for 15 min at RT. After fixation, cells were washed twice with PBS.

Image acquisition was controlled by AcquireSR, and the following parameters were used: TIRF for light path, simultaneous for image mode, 90 for ring size, 512 × 512 for image size, 1 × 1 for binning and 286 MHz for readout speed. Suitable cells were identified using 488-nm excitation laser at low percentage of transmission (1%T) in combination with an AF488 emission filter. Empirically, a cell with maximal intensity ~250–350 (~2500–3500 if the beam concentrator was on) under 75-ms exposure was at the good level of transfection that gave rise to high labeling density but without over-expression artifacts. The beam concentrator was then turned on and reference TIRFM images were acquired using the above setting. Before PALM acquisition, the sample was illuminated with 561-nm excitation laser at 100%T to bleach spontaneously activated fluorophores or background autofluorescence. For each PALM activation/acquisition cycle, 1 ms of 405-nm activation laser was pulsed without continuous illumination, and then five images were acquired using 30-ms exposure of 561-nm excitation laser at 100%T. The power of 405-nm activation laser was increased as the acquisition proceeded. Focus drift during acquisition was corrected either manually or by the HW UltimateFocus autofocus module. Under such experimental setup, ~15,000–25,000 images in total could be collected, which were generally sufficient to generate an acceptable reconstructed data set/image later. Single molecule localization was determined and corrected by softWoRx, and the following parameters were used: (localization) 1.450 for PSF size factor and

with vehicle control or 5 μM LatB for 30 min, and then stimulated to trigger SOCE. ER Ca²⁺ store was depleted with 100 μM His and 1 μM Tg; extracellular Ca²⁺ was chelated with 3 mM EGTA and later added back with 2 mM CaCl₂. Fura-2 intensities at 340-/380-nm excitation were recorded. Intensity ratios for Fura-2 are plotted. Curve and bars: mean with 95% CI (*n* = 4 experiments; the number of cells measured in each experiment was as follows: 327, 331, 420 and 316 for Ctrl; 417, 289, 415, 344 for LatB). *p* Value from paired two-tailed Student's *t* test at each time point during the SOCE is reported.

0.01 for localization maximum factor; (image correlation drift correction) 15 s for time window and 20 nm for pixel size; (tracking/multiple-blinking identification) 20 nm for maximum localization precision, 10 nm for search radius, and one frame for fluorophore off time. The output localization data sets were used for further data analysis described under *Image and data analysis*. Conventional PALM images were reconstructed by softWoRx with the following parameters: Gaussian for reconstruction method, 5 and 20 nm for min/max localization precision, respectively, and one and one frame for min/max fluorophore persistence, respectively.

TIRFM imaging

TIRFM imaging was performed with a custom-built system (Solamere Technology Group, Salt Lake City, UT) based on a Nikon Eclipse Ti-E inverted microscope (Nikon Instruments, Melville, NY). Micro-Manager (Edelstein *et al.*, 2010) was used to control the system. Images were taken with a CFI Apo TIRF 100× oil objective or a CFI Plan Apo Lambda 100× oil objective (Nikon Instruments, Melville, NY) and a CoolSNAP HQ2 charge-coupled device (CCD) camera (Photometrics, Tucson, AZ).

For TIRFM imaging experiments, HeLa cells or HeLa cells stably expressing MAPPER were seeded on an eight-well Nunc Lab-Tek chambered coverglass at a density of 2×10^4 cells/well 1 d before transfection. Plasmid DNA was transfected into cells with TransIT-X2 or TransIT-LT1 (Mirus Bio, Madison, WI) using 1:2 or 1:3 DNA-to-reagent ratio, respectively. The following amounts of plasmid DNA were used for experiments: 25 ng/well of GFP-PLC δ -PH, 30 ng/well of YFP-KRas-tail or mCherry-KRas-tail, 50 ng/well of MAPPER, 50 ng/well of Nir2-mCherry, 50 ng/well of mCherry-STIM1, and 75 ng/well of H1R. Titrations of LatB was done and 5 μ M LatB was determined to be able to disrupt cortical actin without compromising cell attachment for the majority of cells (data not shown). Except for Nir2 translocation and PM PI(4,5)P $_2$ replenishment assays, cells were treated with drugs or vehicle control (if specified) for 30 min at 37°C in a 5% CO $_2$ incubator before proceeding to live cell imaging or fixation. Alexa Fluor 568-Phalloidin (Thermo Fisher Scientific, Waltham, MA) staining was performed according to the manufacturer's instructions except that 150 μ l/well of staining solution at 400× dilution was used. For live cell imaging, cells were washed once with ECB and equilibrated in ECB at RT for 10 min before imaging. For Nir2 translocation or PM PI(4,5)P $_2$ replenishment assays, cells overexpressing H1R together with Nir2-mCherry or GFP-PLC δ -PH were treated with LatB or vehicle control 15 min before experiments. Histamine (100 μ M) was applied to induce PI(4,5)P $_2$ depletion by H1R stimulation.

SIM imaging

SIM imaging was performed with a DeltaVision OMX SR imaging system equipped with a PLAPON 60× oil objective and a pco.edge sCMOS camera.

For TIRF-SIM imaging experiments, HeLa cells stably expressing MAPPER were seeded on an eight-well Nunc Lab-Tek II chambered coverglass at a density of 2×10^4 cells/well ~40 h before staining. Alexa Fluor 568-Phalloidin staining was performed before imaging according to the manufacturer's instructions except that 150 μ l/well of staining solution at 400× dilution was used.

Image acquisition was controlled by AcquireSR, and the following parameters were used: SI TIRF for light path, sequential for image mode, 90 for ring size, 512 × 512 for image size, 1 × 1 for binning, and 286 MHz for readout speed. Suitable cells were identified using 488-nm and 568-nm excitation lasers in combination with AF488 and AF568 emission filters, respectively. Before TIRF-SIM

acquisition, the beam concentrator was turned on. For each reconstruction in each channel, the TIRF illumination plane was imaged at three phase shifts in three angles. Images were acquired using 10–20-ms exposure of 488- or 561-nm excitation lasers at 5–20%T. Image reconstruction was performed with softWoRx, and the following parameters were used: SI-TIRF- and channel-specific OTFs and k0 angles, 0.003 for Wiener filter constant, and 30 for bias offset. The reconstruction option "Discard negative intensities" was disabled according to the guideline suggested by Demmerle *et al.* (2017). Channel alignment was done using parameters generated from a gold grid registration slide (GE Healthcare, Pittsburgh, PA) and the OMX Image Registration Calibration tool in SoftWoRx. Background subtraction and brightness/contrast adjustment of the reconstructed images was performed in ImageJ distribution Fiji (Schindelin *et al.*, 2012).

Ca $^{2+}$ imaging

Ca $^{2+}$ imaging was performed as previously described (Chang *et al.*, 2013). Fura-2 loaded cells were treated with LatB or vehicle control 30 min before imaging experiments.

Image and data analysis

ImageJ/Fiji was used to measure lengths of ER-PM junctions from electron micrographs. ER-PM junctions were visually identified as the regions where the gap distance between the ER and the PM is smaller than 20 nm.

An integrated software platform developed by Levet *et al.* (2015) was used to extract quantitative information about the morphology of ER-PM junctions from PALM data sets. Those interested in the associated analysis methods are advised to read the original article by Levet *et al.* (2015) and a nice review by Nicovich *et al.* (2017). Localization data sets generated by softWoRx of DeltaVision OMX SR imaging system were first reformatted and cleaned using a custom MATLAB (MathWorks, Natick, MA) function. Essentially, molecules satisfying one of the following criteria were removed: 1) derived from frames with poor lateral drift correction (rarely happens if the acquisition/localization is terminated before activated fluorophores become too sparse), 2) with localization precision greater than 20 nm, or 3) identified as repetitive detections due to multiple blinking. Also, to achieve better consistency when performing Ripley's *K* analysis and image segmentation by SR-Tesseler, a region of interest (ROI) covered by the cell was cropped from each localization data set. Ripley's *K* analysis was performed within the platform, which implements an algorithm optimization based on the Voronoï diagram. The radius of maximal aggregation in each localization data set was identified with two iterations of analysis using step sizes 10 and 1 nm. Voronoï-based segmentation was obtained using the following parameters: density cutoff = 2 and minimal localizations per object = 100. DBSCAN was also performed within the platform and the following parameters were used: search radius ϵ = 50 nm, minimal localizations per neighborhood = 50 and minimal localizations per object = 100. Equivalent diameters of objects were calculated from the areas reported by SR-Tesseler, using the formula $2\sqrt{\text{area}/\pi}$. Principal component analysis was performed, and major and minor axes of objects were normalized from the SDs along principal components by a factor 3.2897, equivalent to 90% of a Gaussian distribution. Aspect ratios were calculated using the formula *major axis/minor axis*.

ImageJ/Fiji, ilastik 1.2.2rc4 (Sommer *et al.*, 2011) and MATLAB R2016b were used to assess the spatial relationship between ER-PM junctions and cortical actin. ROIs containing individual cells were

cropped from raw TIRFM or reconstructed TIRF-SIM images, converted to 16-bit TIFF images, and subjected to background subtraction using ImageJ/Fiji. Next, the distribution/localization of F-actin structures was identified using pixel classification workflow of ilastik. Classifiers were separately trained to segment F-actin structures from the background using representative data sets of both TIRFM and TIRF-SIM images, and then the trained classifiers were used to segment all of the images. Locations of ER-PM junctions were determined by LoG detector built in TrackMate (Tinevez *et al.*, 2017) plug-in of ImageJ/Fiji. Output data sets from both ilastik and TrackMate were then analyzed using MATLAB. Briefly, if the center of an ER-PM junction fell within segmented F-actin regions and was >1.5-pixel away (in L_1 -norm) from the nearest background region, this junction was considered as superimposed on F-actin. Otherwise, the distance (in L_2 -norm) from the center of an ER-PM junction to the nearest segmented F-actin region was measured.

ImageJ/Fiji and MATLAB R2016b were used to assess the density and subcellular distribution of ER-PM junctions. For a given raw TIRFM image, background was subtracted, ROIs were determined by PM staining of mCherry-KRas-tail, and ER-PM junctions were localized using LoG detector built in TrackMate plug-in of ImageJ/Fiji. Output data sets were further analyzed using MATLAB.

ImageJ/Fiji and MATLAB R2016b were used to characterize lateral motility of ER-PM junctions. Junctions were localized using LoG detector and tracked using a simple LAP tracker (Jaqaman *et al.*, 2008) built-in TrackMate plug-in of ImageJ/Fiji. MSD analysis was performed with MATLAB class msdalyzer (Tarantino *et al.*, 2014).

Quantification of $PI(4,5)P_2$ level at the PM during receptor stimulation was performed as previously described (Chang and Liou, 2015). Briefly, TIRFM images were analyzed with MetaMorph (Molecular Devices, Sunnyvale, CA) to obtain relative change of GFP-PLC δ -PH intensity from single cells.

Quantification of STIM1 translocation following thapsigargin was performed as previously described (Chen *et al.*, 2017). Briefly, TIRFM images were analyzed with MetaMorph to obtain relative change of mCherry-STIM1 intensity from single cells.

Quantification of intracellular Ca^{2+} level during ER Ca^{2+} depletion and SOCE was performed as previously described (Liou *et al.*, 2005). Briefly, widefield fluorescence images were analyzed with MetaMorph to obtain F340/F380 change from single cells.

Data visualization and statistical analysis were performed with MATLAB R2016b or GraphPad Prism 7 (GraphPad Software, La Jolla, CA).

All custom MATLAB scripts and functions used in this study are available on request.

ACKNOWLEDGMENTS

We thank Loren Looger of Janelia Research Campus for providing the mEos4 construct; Tobias Meyer of Stanford University for providing GFP-PLC δ -PH, YFP-KRas-tail, and mCherry-KRas-tail constructs; Elliott Ross for providing the H1R construct; Patrina Pellett of GE Healthcare and Katherine Luby-Phelps of UTSW Live Cell Imaging Core Facility for assistance on DeltaVision OMX SR; the UTSW Electron Microscopy Core Facility for assistance on TEM experiments; Florian Levot of University of Bordeaux for assistance on SR-Tesseler; Khuloud Jaqaman for discussion on data analysis and input on the manuscript; and Linda Patterson for administrative assistance. This work was supported by Welch Foundation Grant I-1789 and by National Institutes of Health Grant GM113079 to J.L. J.L. is a Sowell Family Scholar in Medical Research.

REFERENCES

- Chang CL, Chen YJ, Liou J (2017). ER-plasma membrane junctions: why and how do we study them? *Biochim Biophys Acta* 1864, 1494–1506.
- Chang CL, Hsieh TS, Yang TT, Rothberg KG, Azizoglu DB, Volk E, Liao JC, Liou J (2013). Feedback regulation of receptor-induced Ca^{2+} signaling mediated by E-Syt1 and Nir2 at endoplasmic reticulum-plasma membrane junctions. *Cell Rep* 5, 813–825.
- Chang CL, Liou J (2015). Phosphatidylinositol 4,5-bisphosphate homeostasis regulated by Nir2 and Nir3 proteins at endoplasmic reticulum-plasma membrane junctions. *J Biol Chem* 290, 14289–14301.
- Chen YJ, Chang CL, Lee WR, Liou J (2017). RASSF4 controls SOCE and ER-PM junctions through regulation of $PI(4,5)P_2$. *J Cell Biol* 216, 2011–2025.
- Clark PJ, Evans FC (1954). Distance to nearest neighbor as a measure of spatial relationships in populations. *Ecology* 35, 445–453.
- Demmerle J, Innocent C, North AJ, Ball G, Muller M, Miron E, Matsuda A, Dobbie IM, Markaki Y, Schermelleh L (2017). Strategic and practical guidelines for successful structured illumination microscopy. *Nat Protoc* 12, 988–1010.
- Dingsdale H, Okeke E, Awais M, Haynes L, Criddle DN, Sutton R, Tepikin AV (2013). Saltatory formation, sliding and dissolution of ER-PM junctions in migrating cancer cells. *Biochem J* 451, 25–32.
- Edelstein A, Amodaj N, Hoover K, Vale R, Stuurman N (2010). Computer control of microscopes using μ Manager. *Curr Protoc Mol Biol* 92, 14.20.1–14.20.17.
- Eghiaian F, Rigato A, Scheuring S (2015). Structural, mechanical, and dynamical variability of the actin cortex in living cells. *Biophys J* 108, 1330–1340.
- Ester M, Kriegel H-P, Sander J, Xu X (1996). A density-based algorithm for discovering clusters in large spatial databases with noise. In: *Proceedings of the Second International Conference on Knowledge Discovery and Data Mining (KDD-96)*, ed. E Simoudis, J Han, and U Fayyad, Palo Alto, CA: AAAI Press, 226–231.
- Fernandez-Busnadiego R, Saheki Y, De Camilli P (2015). Three-dimensional architecture of extended synaptotagmin-mediated endoplasmic reticulum-plasma membrane contact sites. *Proc Natl Acad Sci USA* 112, E2004–E2013.
- Giordano F, Saheki Y, Idevall-Hagren O, Colombo SF, Pirruccello M, Milosevic I, Gracheva EO, Bagriantsev SN, Borgese N, De Camilli P (2013). $PI(4,5)P_2$ -dependent and Ca^{2+} -regulated ER-PM interactions mediated by the extended synaptotagmins. *Cell* 153, 1494–1509.
- Heo WD, Inoue T, Park WS, Kim ML, Park BO, Wandless TJ, Meyer T (2006). $PI(3,4,5)P_3$ and $PI(4,5)P_2$ lipids target proteins with polybasic clusters to the plasma membrane. *Science* 314, 1458–1461.
- Jaqaman K, Loerke D, Mettlen M, Kuwata H, Grinstein S, Schmid SL, Danuser G (2008). Robust single-particle tracking in live-cell time-lapse sequences. *Nat Methods* 5, 695–702.
- Jozsef L, Tashiro K, Kuo A, Park EJ, Skoura A, Albinsson S, Rivera-Molina F, Harrison KD, Iwakiri Y, Toomre D, Sessa WC (2014). Reticulon 4 is necessary for endoplasmic reticulum tubulation, STIM1-Orai1 coupling, and store-operated calcium entry. *J Biol Chem* 289, 9380–9395.
- Kim YJ, Guzman-Hernandez ML, Wisniewski E, Balla T (2015). Phosphatidylinositol-phosphatidic acid exchange by Nir2 at ER-PM contact sites maintains phosphoinositide signaling competence. *Dev Cell* 33, 549–561.
- Kiskowski MA, Hancock JF, Kenworthy AK (2009). On the use of Ripley's K-function and its derivatives to analyze domain size. *Biophys J* 97, 1095–1103.
- Kronlage C, Schafer-Herte M, Boning D, Oberleithner H, Fels J (2015). Feeling for filaments: quantification of the cortical actin web in live vascular endothelium. *Biophys J* 109, 687–698.
- Levet F, Hosy E, Kechkar A, Butler C, Beghin A, Choquet D, Sibarita JB (2015). SR-Tesseler: a method to segment and quantify localization-based super-resolution microscopy data. *Nat Methods* 12, 1065–1071.
- Liou J, Kim ML, Heo WD, Jones JT, Myers JW, Ferrell JE Jr, Meyer T (2005). STIM is a Ca^{2+} sensor essential for Ca^{2+} -store-depletion-triggered Ca^{2+} influx. *Curr Biol* 15, 1235–1241.
- Morone N, Fujiwara T, Murase K, Kasai RS, Ike H, Yuasa S, Usukura J, Kusumi A (2006). Three-dimensional reconstruction of the membrane skeleton at the plasma membrane interface by electron tomography. *J Cell Biol* 174, 851–862.
- Nan X, Collisson EA, Lewis S, Huang J, Tamguney TM, Liphardt JT, McCormick F, Gray JW, Chu S (2013). Single-molecule superresolution imaging allows quantitative analysis of RAF multimer formation and signaling. *Proc Natl Acad Sci USA* 110, 18519–18524.
- Nicovich PR, Owen DM, Gaus K (2017). Turning single-molecule localization microscopy into a quantitative bioanalytical tool. *Nat Protoc* 12, 453–460.

- Okeke E, Dingsdale H, Parker T, Voronina S, Tepikin AV (2016). Endoplasmic reticulum-plasma membrane junctions: structure, function and dynamics. *J Physiol* 594, 2837–2847.
- Orci L, Ravazzola M, Le Coadic M, Shen WW, Demaurex N, Cosson P (2009). STIM1-induced precortical and cortical subdomains of the endoplasmic reticulum. *Proc Natl Acad Sci USA* 106, 19358–19362.
- Paez-Segala MG, Sun MG, Shtengel G, Viswanathan S, Baird MA, Macklin JJ, Patel R, Allen JR, Howe ES, Piszczek G, et al. (2015). Fixation-resistant photoactivatable fluorescent proteins for CLEM. *Nat Methods* 12, 215–218.
- Saheki Y, De Camilli P (2017). Endoplasmic reticulum-plasma membrane contact sites. *Annu Rev Biochem* 86, 659–684.
- Schindelin J, Arganda-Carreras I, Frise E, Kaynig V, Longair M, Pietzsch T, Preibisch S, Rueden C, Saalfeld S, Schmid B, et al. (2012). Fiji: an open-source platform for biological-image analysis. *Nat Methods* 9, 676–682.
- Sommer C, Straehle C, Kothe U, Hamprecht FA (2011). ilastik: Interactive Learning and Segmentation Toolkit. In: *Proceedings of 2011 IEEE International Symposium on Biomedical Imaging: From Nano to Macro (ISBI'11)*, 230–233.
- Stauffer TP, Ahn S, Meyer T (1998). Receptor-induced transient reduction in plasma membrane PtdIns(4,5)P₂ concentration monitored in living cells. *Curr Biol* 8, 343–346.
- Tarantino N, Tinevez JY, Crowell EF, Boisson B, Henriques R, Mhlanga M, Agou F, Israel A, Laplantine E (2014). TNF and IL-1 exhibit distinct ubiquitin requirements for inducing NEMO-IKK supramolecular structures. *J Cell Biol* 204, 231–245.
- Tinevez JY, Perry N, Schindelin J, Hoopes GM, Reynolds GD, Laplantine E, Bednarek SY, Shorte SL, Eliceiri KW (2017). TrackMate: an open and extensible platform for single-particle tracking. *Methods* 115, 80–90.
- van Vliet AR, Giordano F, Gerlo S, Segura I, Van Eygen S, Molenberghs G, Rocha S, Houcine A, Derua R, Verfaillie T, et al. (2017). The ER stress sensor PERK coordinates ER-plasma membrane contact site formation through interaction with filamin-A and F-actin remodeling. *Mol Cell* 65, 885–899.e6.
- Wang P, Hawkins TJ, Richardson C, Cummins I, Deeks MJ, Sparkes I, Hawes C, Hussey PJ (2014). The plant cytoskeleton, NET3C, and VAP27 mediate the link between the plasma membrane and endoplasmic reticulum. *Curr Biol* 24, 1397–1405.
- West M, Zurek N, Hoenger A, Voeltz GK (2011). A 3D analysis of yeast ER structure reveals how ER domains are organized by membrane curvature. *J Cell Biol* 193, 333–346.
- Wu MM, Buchanan J, Luik RM, Lewis RS (2006). Ca²⁺ store depletion causes STIM1 to accumulate in ER regions closely associated with the plasma membrane. *J Cell Biol* 174, 803–813.
- Wu Y, Whiteus C, Xu CS, Hayworth KJ, Weinberg RJ, Hess HF, De Camilli P (2017). Contacts between the endoplasmic reticulum and other membranes in neurons. *Proc Natl Acad Sci USA* 114, E4859–E4867.
- Xu K, Babcock HP, Zhuang X (2012). Dual-objective STORM reveals three-dimensional filament organization in the actin cytoskeleton. *Nat Methods* 9, 185–188.
- Zhang D, Bidone TC, Vavylonis D (2016). ER-PM contacts define actomyosin kinetics for proper contractile ring assembly. *Curr Biol* 26, 647–653.